Selective grating obtained by dye micro-structuration based on local photo- bleaching using laser writer

Alban Gassenq, Kevin Chevrier, Antoine Bard, Jean-Michel Benoit, Clémentine Symonds, Joël Bellessa

Selective grating obtained by dye micro-structuration based on local photo- bleaching using laser writer

Jean Michel Benoit, Alban Gassenq, Kevin Chevrier, Antoine Bard, Jean-Michel Benoit, Clementine Symonds, Joel Bellessa

To be published in Applied Optics:

Title: Selective grating obtained by dye micro-structuration based on local photo-bleaching using laser writer

Authors: Alban Gassenq,Kevin CHEVRIER,Antoine BARD,jean michel benoit,Clementine Symonds,Joel Bellessa

Accepted: 01 June 20

Posted 02 June 20

DOI: https://doi.org/10.1364/AO.393103

Selective grating obtained by dye micro-structuration based on local photo-bleaching using laser writer

ALBAN GASSENQ,[1,*] KEVIN CHEVRIER,[1] ANTOINE BARD,[1] JEAN-MICHEL BENOIT,[1] CLEMENTINE SYMONDS,[1] AND JOEL BELLESSA,[1]

[1] *Univ Lyon, Université Claude Bernard Lyon 1, CNRS, Institut Lumière Matière, UMR5306, F-69622, LYON, France.*

**Corresponding author: alban.gasseng@univ-lyon1.fr*

Received XX Month XXXX; revised XX Month, XXXX; accepted XX Month XXXX; posted XX Month XXXX (Doc. ID XXXXX); published XX Month XXXX

We propose a method to pattern organic optically active materials based on local photo-bleaching for making wavelength selective grating. Usually, photo-bleaching is considered as a limitation for organic emitter. Here, this property is exploited to locally suppress dye emission and absorption at the microscale with abrupt interface and no changes in layer thickness. Periodic patterns were fabricated and exhibit diffraction only at 590nm wavelength with spectral selectivity of 11nm. Based on laser writer flexibility and efficiency, this study shows the potential of local photo-bleaching for several applications like wavelength selective grating fabrication.

http://dx.doi.org/XXXXXX/XXXXXXXX

1. Introduction

The patterning of optically active organic materials is a key feature for numerous applications involving organic emitters. Patterning organic materials is usually achieved using soft lithography processes [1,2], since conventional photolithography techniques used in microelectronics are often non compatible with sensitive materials [3]. Nevertheless, soft lithography often requires complex layers transfer and surface chemistry, depending on the envisioned device structure. Dye photo-bleaching represents an alternative method for structuration. Usually, photo-bleaching is considered as a limitation for organic emitter [4,5]. But, this property can be exploited to suppress dye emission and absorption [6] which can be used for controlling the dye properties for strong coupling application [7]. In this work we propose a new method based on local photo-bleaching [7,8] of dye layers to obtain micro-structured organic material without complex lithography processing. In addition, we exploit an industrial laser writer to locally photo-bleach the material. Like all mask less lithography methods (e.g. spatial light modulators based lithography [9,10]), this very versatile technique allows an easy fabrication of any kind of micro-structured flat geometry.

Moreover, one of the main interest of the photo-bleaching approach is that it only alters the optical index in the wavelength range of the absorption [7]. The obtained structuration is thus strongly wavelength dependent. To validate the efficiency of our method, we propose to apply this concept to the fabrication of wavelength selective gratings of different shapes and periods. This easy processing technique could be a convenient alternative to the previously described methods [11–15] for selective wavelength grating fabrication, such as multiple interference [11–13], cholesteric liquid crystal [14,15] or plasmonic system [16,17].

In the first part of this paper, we will show that such technique allows to locally remove absorption and photoluminescence in insolated layers at the macro scale. We then study the influence of insolation dose by fluorescence, bright and dark field imaging on micro-scale patterns. Finally, we will focus on periodically insolated dye patterns, and investigate their wavelength selective diffraction properties.

2. Fabrication

Samples consist of locally photo-bleached dye deposited on thin silver film on glass substrate. Figure 1 presents the process flow for the sample fabrication. A 50 nm thick silver layer was thermally evaporated on glass substrate, and an aqueous solution of J-aggregated dye TDBC (5,6-Dichloro-2-[[5,6-dichloro-1-ethyl-3-(4-sulfobutyl)-benzimidazol-2-ylidene]-propenyl]-1-ethyl-3-(4-sulfobutyl)-benzimidazolium hydroxide, inner salt, sodium salt) is spin coated on top of the silver film (Figure 1-a). The concentration of the TDBC aqueous solution is 8.39×10^{-3} M. This active molecule on silver has been chosen because it is widely used in strong coupling studies [7,18,19]. The spin coated layer has a 17 nm thickness measured by plasmon fitting [7]. Finally, µPG101 laser writer with 365 nm wavelength was used for the local insolation. The laser spot was focused on a ~0.5 μm^2 surface, with an adjustable laser power up to 70 mW. A writing speed of 1 mm^2/min was used resulting in a maximum insolation dose of 110 J/cm^2. Design files were programed with GDSpy python library for providing patterns to the laser lithography machine. In order to prevent sample from oxidation and ambient light photo-bleaching, samples were kept under vacuum in dark environment. Using such precaution, dye patterning is still observed several months after fabrication and characterizations.

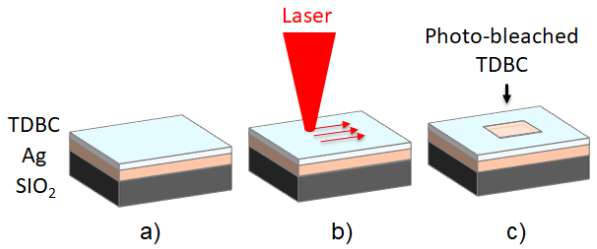

Fig. 1. Process flow for the sample fabrication starting from a glass substrate with first a) Ag deposition by evaporation and TDBC spin coating followed by b) the laser insolation giving c) micro-bleached patterning.

3. Optical characterizations

Figure 2 shows absorption and photoluminescence spectra of such TDBC layers deposited on silver with or without photo-bleaching. Absorbance was measured with a Perkin Elmer lambda 900 spectrometer. Photoluminescence measurement was performed under low excitation (<2 mW/cm²) using a 532 nm wavelength laser with a 400 µm² spot size. Sample was insolated at ~100 J/cm² on a surface larger than the detection area. Before insolation, a narrow absorption line around 2.1 eV is observed associated with a photoluminescence peak at 2.08 eV, in good agreement with TDBC properties [20]. After insolation, neither emission nor absorption are observed [18,21].

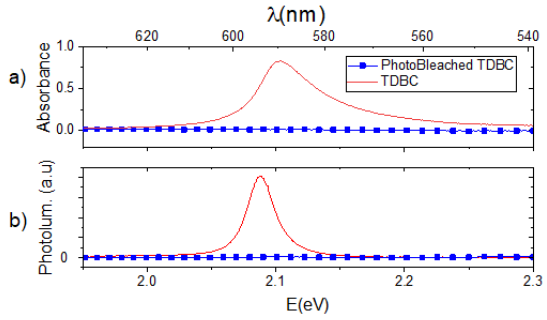

Fig. 2. a) Absorption and b) Photoluminescence measurements for photobleached and un-photobleached sample

Figure 3-a presents top view imaging of a patterned layer insolated at 40 J/cm². The theoretical design is a 11 µm width rectangle. Optical properties of the samples were studied by microscopy using dark field (DF), fluorescence (Fluo.) and Bright Field (BF) imaging with a x50 objective. For all images, two regions are clearly observed: the insolated region (in the middle of the Figure 3-a) and the un-insolated region (all around the insolated region). In BF observation, the un-insolated region is blue because TDBC layer absorbs mainly red wavelengths (Figure 2-a). The insolated region appears pale yellow, which corresponds to the metal below the insolated layer because the photo-bleached layer is transparent after photo-bleaching. For Fluorescence, insolated region appears black because the layer emission is suppressed by photo-bleaching and un-insolated region is orange because emission is localized at around 590 nm (Figure 2-b). For DF imaging (acquisition time x100 compared to BF and Fluo.), some white spots are present in both regions attributed to light scattered by defects. A contrast between both regions is also observed, as the un-insolated region appears in dark orange due to TDBC light scattering [22] and in-plane fluorescence. Using ImageJ software, gray scale along the X direction and normalized contrast were measured. The pattern width (W in the Figure 3-b) was measured at the half maximum contrast. The deviation from the target width is estimated by $\Delta W = W - W_{th}$, with W_{th} the theoretical design programmed in the GDS file (W_{th} = 11 µm). The normalized contrast (C in the Figure 3-b) is calculated with $C = (I_0 - I_{photo})/I_0$ with I_0 the maximal image intensity in the un-photobleached region and I_{photo} the minimal intensity in the photo-bleached region. Figures 3-c and -d present ΔW and C as a function of insolation dose. For BF imaging, "–C" has been plotted for easier comparison.

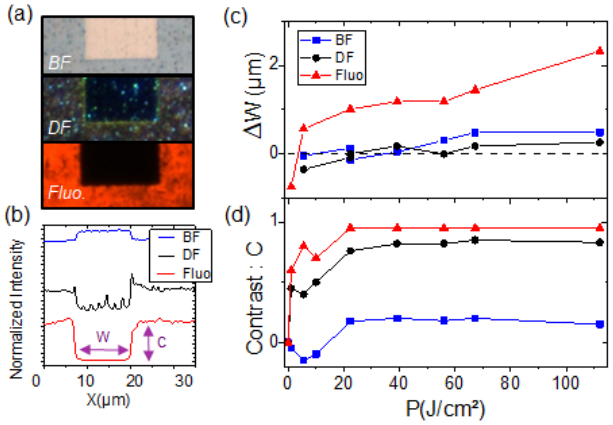

Fig 3. a) Optical images of the fabricated sample and b) associated normalized grey scale; c) pattern width difference and d) image contrast as a function of the insolation dose.

For low insolation dose (<20 J/cm²), the dye is not fully photo-bleached as indicated by the low contrast values (Figure 3-d). The contrast then increases with the insolation dose up to saturation. Even if saturation is reached at the same dose for all imaging mode, the measured contrast increases faster with the dose in the case of Fluorescence and DF imaging compared to BF imaging. This could be explained by a smaller dose needed to bleach emission compared to absorption [23]. Above 20 J/cm², the contrast remains high and stable as a function of the used dose, which indicates a complete photo-bleaching of the layer. Note that the needed dose to reach photo-bleaching could be reduced using wavelength with higher TDBC absorption [24]. Concerning the pattern width, a very good agreement with the target width is found in BF and DF imaging (ΔW<1 µm) with a slightly pattern width increase at very high dose. For fluorescence imaging, larger widths are observed probably due to light diffusion affecting dye emission also in the vicinity of the insolated region. Therefore, the optimal dose to obtain high contrast and small width difference with the theoretical design should be around 40 J/cm².

Figure 4-a presents a zoom on the transition between un-insolated and insolated regions (dose 40 J/cm²) using fluorescence, BF and DF microscopy. On the normalized grey profiles (Figure 4-b), the transition length was evaluated to be below 1µm with light scattering detected at the interface in DF imaging indicating abrupt interfaces between both regions. Like reported above, the insolated region appears larger in Fluorescence imaging. In order to evaluate the spatial resolution, we have then insolated very small disks of 500 nm and 1 µm diameters at 40 J/cm². Figure 4-c presents the fabricated samples. Like previously observed (Figure 3-c), we obtain a good correlation with the targeted diameter with a slight increase of the diameter only for fluorescence imaging. We confirm here that we are able to reach micrometric resolution and high contrast with this method.

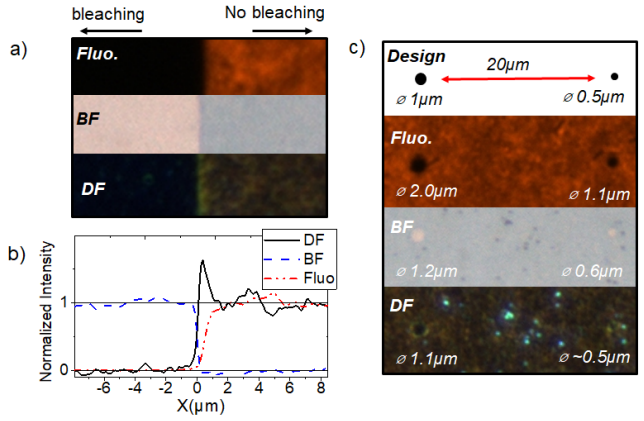

Fig 4. Insolated samples at 40J/cm^2 a) zoom of the transition region between insolated and un-insolated areas in fluorescence, bright field and dark field imaging; b) associated normalized grey profiles; c) images of a sample with 500 nm and 1 µm diameter insolated disks.

4. Wavelength selective grating

Gratings with patterns of different shapes and periods were fabricated, as presented in the optical images of Figure 5-a and b. As a function of the design programing, we can easily choose the grating symmetry (biaxial, triaxial…), filling factor, pattern width, shape, number of period. Figure 5-c presents Atomic Force Microscopy (AFM) measurement for a triaxial design. AFM measurements were performed with a Nanosurf-EasyScan2 equipment with a TAP190AL-G-10 probe in tapping mode. The obtained image was recorded on a surface of 20x20 µm^2 and a Z profile was extracted using Gwyddion software (Figure 5-d). In this measurement, we clearly see that (1) the thickness of the layer is not affected (±2 nm) by the photo-bleaching and (2) small trenches are detected at the interface which explain the light scattering observed at the interface in DF mode (Figure 4-b). These characterizations confirm that our method only affects the absorption/emission properties of the material with abrupt interfaces and no change in the layer thickness between both regions.

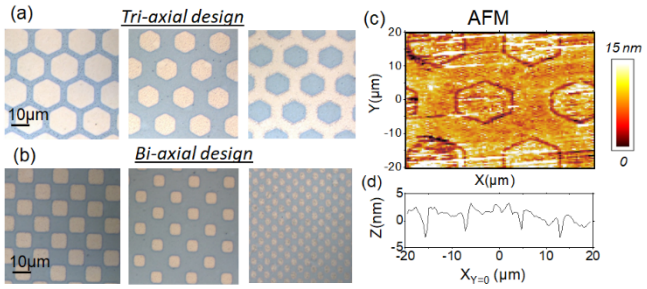

Fig. 5. Image of fabricated samples with periodic micro-structures by a) optical microscopy for a) tri-axial and b) bi-axial designs and by b) AFM microscopy for a tri-axial design with c) the Z profile averaged over Y=±2 µm

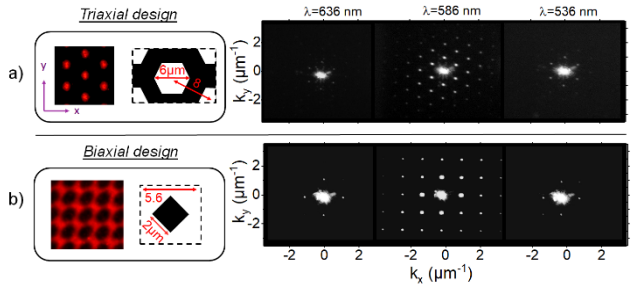

Fig. 6. Fluorescence image, design and associated reflected intensity in the Fourier space with different excitation wavelengths for a) tri-axial and b) bi-axial design samples.

The optical properties of gratings were then investigated. Figure 6 presents reflection measurements of two samples illuminated with 3 different wavelengths, using a supercontinuum source (Leukos) focused on a 1mm^2 spot with a x20 microscope objective (N.A. = 0.5). The scattered light is collected by the same objective, and the Fourier plane is imaged on a CCD camera [25]. This provides a reflectivity image as a function of the wavevector, showing the scattered directions. To measure the scattering of the sample, a well-defined excitation is necessary, i.e. a quasi-parallel incident beam after the microscope objective. For this purpose, the excitation beam aperture is reduced by inserting a 100 µm pinhole in a plane conjugated with the Fourier plane of the microscope objective. This ensures a perpendicular illumination of the sample with small angle aperture (~8°). Unit cell of the designs are presented on the left side of Figure 6 with associated fluorescence images. The Fourier space images show for both designs a strong diffraction at 586 nm that vanishes for higher and lower wavelengths (536 and 636 nm). Due to the silver surface, a reflectivity at 0 order is present, reflectivity which would be there even without grating. Therefore, for usual grating, light diffraction occurs at all wavelength. In this so called "wavelength selective grating" device, diffraction occurs only at around 590 nm. Indeed, since photo-bleaching affects the real and imaginary parts of the TDBC refractive index only at around 590 nm wavelength [7], the grating effect occurs only in this spectral range (Figure 2-b).

For the tri-axial design, 6 µm wide hexagons were insolated with 8µm period (Fig 6-a), several diffraction orders organized in a triangular lattice are observed for a 586 nm excitation. The distance between the first peaks and the central spot is 0.86 µm^{-1}, in good agreement with the 8 µm real space period (2π/period=7.3 µm^{-1}). For the biaxial design, 2 µm wide squares were insolated with a 5.6 µm period. In that case the obtained diffraction peaks are organized in a square lattice. The distance between the central and the first diffraction order is 1.29 µm^{-1}, also in good agreement with the 5.6 µm real space period (2π /period=4.9 µm^{-1}).

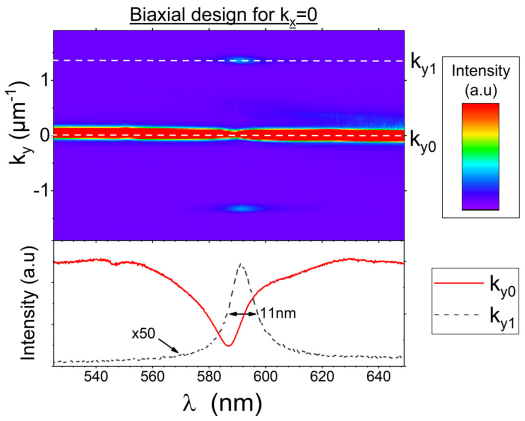

Fig. 7. (top panel) Reflected light for the square array as a function of the wavelength and the k_y wavevector at k_x=0 μm^{-1}. (bottom panel) Intensity profile at k_{y0}=0 and k_{y1}=1.2 μm^{-1}.

To go deeper in the analysis of the optical properties of these gratings, spectral characterization of the reflectivity has been performed. The Figure 7 presents the reflected intensity as a function of the wavelength and the wavevector along the y direction. The image of the Figure 7 corresponds to the selection of a vertical line (at k_x=0) in the image of Figure 6-b with the wavelength as horizontal axis. For this purpose, the sample is illuminated with a white source, in the same configuration as described above. The Fourier plane of the objective is now imaged on the entrance slit of a spectrometer, which selects a vertical line at k_x=0μm^{-1} in the corresponding reflectometry images of Figure 6. The resulting spectral image shows the reflected intensity as a function of the wavelength and the vertical wavevector k_y, as presented in Figure 7 for the bi-axial design. A spectrally broad reflectivity is measured all along the normal direction (k_y~0 μm^{-1}) corresponding to the zero order diffraction. A dip at 586 nm can be associated to the dye absorption/scattering. Furthermore, at 589 nm two scattered peaks appear at k_y=+-1.2 μm^{-1}. This corresponds to a 2π/k=5.2 μm period, which is in good agreement with the fabricated sample (Figure 6-b). It has to be noticed that the minimum in the zero order peak is not at the same wavelength as the maximal scattered light. This could be attributed to the difference between the absorption, mainly associated with the imaginary part of the index, and the scattering associated with variation of the real part. The same wavelength difference is observed in metallic nanoparticles scattering/absorption [6]. Such wavelength offset between absorption and diffraction would be obviously a drawback for wavelength selective filter application but which can be accepted as tradeoff since devices are compact and highly selective. Indeed, the sharp linewidth (full width at half maximum of 11 nm) of the scattered spectrum shows the interest of this method for wavelength selective gratings.

5. Conclusion

To sum up, we have shown that versatile active dye micro-structuration can be obtained using laser writer. This method allows relatively fast and large-scale dye micro-structuration using reliable industrial equipment. We have periodically insolated dye on silver showing many patterning possibilities for wavelength selective grating fabrication. This work thus highlights the high potential of the local-photo-bleaching method for obtaining many kind of micro-structured geometries in organic emitters, and could be applied for different applications like strong coupling studies [6,7,19,26] or wavelength selective grating [11–15,17].

Acknowledgment. The authors would like to thank the Nanolyon Platform for clean room facilities and the ANR Plashybrid project for funding (ANR-18-CE30-0014).

Disclosures. The authors declare no conflicts of interest.

References

1. P. Kim, K. W. Kwon, M. C. Park, S. H. Lee, and S. M. Kim, "Soft Lithography for Microfluidics : a Review," BIOCHIP J. **2**, 1–11 (2008).
2. Y. K. Kwon, K. Han, M. Lee, S. Ko, H. Oh, H. Lee, and E. Lee, "Organic – inorganic hybrid materials for flexible optical waveguide applications," J. Mater. Chem. **18**, 579–585 (2008).
3. D. Li, C. Symonds, F. Bessueille, J. C. Plenet, A. Errachid, G. Wu, J. Shen, and J. Bellessa, "Transfer of optically active polyelectrolyte multilayers by micro-contact printing," J. Opt. A Pure Appl. Opt. **11**, 065601 (2009).
4. T. Ha and P. Tinnefeld, "Photophysics of Fluorescent Probes for Single-Molecule Biophysics and Super-Resolution Imaging," Annu. Rev. Phys. Chem **63**, 595–617 (2012).
5. B. H. Cumpston and K. F. Jensen, "Photo-oxidation of polymers used in electroluminescent devices," Synth. Met. **73**, 195–199 (1995).
6. G. Zengin, P. Johansson, T. J. Antosiewicz, M. Ka, and T. Shegai, "Approaching the strong coupling limit in single plasmonic nanorods interacting," Sci. Rep. **3**, 1–8 (2013).
7. K. Chevrier, J. M. Benoit, C. Symonds, S. K. Saiki, J. Y. Zhou, and J. Bellessa, "Anisotropy and Controllable Band Structure in Suprawavelength Polaritonic Metasurfaces," Phys. Rev. Lett. **122**, 173902 (2019).
8. T. Hattori, T. Shibata, S. Onodera, T. Kaino, T. Hattori, T. Shibata, S. Onodera, and T. Kaino, "Fabrication of refractive index grating into azo-dye-containing polymer films by irreversible photoinduced bleaching," J. Appl. Phys. **87**, 3240 (2006).
9. Y. Liu, Y. Zhao, X. Dong, M. Zheng, F. Jin, J. Liu, X. Duan, Y. Liu, Y. Zhao, X. Dong, and M. Zheng, "Multi-scale structure patterning by digital-mask projective lithography with an alterable projective scaling system Multi-scale structure patterning by digital-mask projective lithography with an alterable projective scaling system," AIP Adv. **8**, 065317 (2018).
10. Y. Hang, J. Uo, Z. Xiong, H. Liu, L. Wang, G. Yingying, L. Zifeng, L. Jinhuan, and H. Jipeng, "User-defined microstructures array fabricated by DMD based multistep lithography with dose modulation," Opt. Express **27**, 31956–31966 (2019).
11. I. Rashid, H. Butt, A. K. Yetisen, B. Dlubak, J. E. Davies, P. Seneor, A. Vechhiola, F. Bouamrane, and S. Xavier, "Wavelength-Selective Di ff raction from Silica Thin-Film Gratings," ACS Photonics **4**, 2402–2409 (2017).
12. Q. He, I. Zaquine, A. Maruani, and R. Frey, "Band-edge-induced Bragg diffraction in two-dimensional photonic crystals," Opt. Lett. **31**, 1184 (2006).
13. M. C. Parker, A. D. Cohen, and R. J. Mears, "Dynamic digital holographic wavelength filtering," J. Light. Technol. **16**, 1259–1269 (1998).
14. H. Chin, H. Kuo, Y. Zheng, J. Lin, and C. Lee, "Circular Polarization and Wavelength Selective Gratings Based on Holographic Cholesteric Liquid Crystal Templates," Adv. Condens. Matter Phys. **384329**, 1–8 (2018).
15. R. OZaki, S. HAshimura, S. YUdate, K. KAdowaki, H. Yoshida, and Ma. OZaki, "Optical properties of selective diffraction from Bragg-Berry cholesteric liquid crystal deflectors," OSA Contin. **2**, 3554–3563 (2019).
16. Y. Gu, L. Zhang, J. K. W. Yang, P. Yeo, and C. Qiu, "Color generation via subwavelength plasmonic nanostructures," Nanoscale **7**, 6409–6419 (2015).
17. Giorgio QUARANTA, "Resonant Waveguide Gratings for Color-Selective Diffraction (phD thesis)," EPFL (2019).

18. B. Munkhbat, M. Wersäll, D. G. Baranov, T. J. Antosiewicz, and T. Shegai, "Suppression of photo-oxidation of organic chromophores by strong coupling to plasmonic nanoantennas," Sci. Adv. **4**, eaas9552 6 (2018).
19. E. S. H. Kang, S. Chen, and S. Sardar, "Strong Plasmon-Exciton Coupling with Directional Absorption Features in Optically Thin Hybrid Nanohole Metasurfaces," ACS Photonics **5**, 4046–4055 (2018).
20. B. W. HOON, I. C. SEO, E. LEE, A. SOO-CHAN, and H. Y. JEONG, "Angle-dependent optical perfect absorption and enhanced photoluminescence in excitonic thin films," Opt. Express **25**, 206–213 (2017).
21. C. Symonds, C. Bonnand, J. C. Plenet, A. Bréhier, R. Parashkov, J. S. Lauret, E. Deleporte, and J. Bellessa, "Particularities of surface plasmon–exciton strong coupling with large Rabi splitting," New J. Phys. **10**, 065017 (2008).
22. R. James, A. Douwe, J. Moll, and S. Daehne, "Optical dynamics of excitons in J aggregates of a carbocyanine dye Optical dynamics of excitons in J aggregates of a carbocyanine dye," J. Chem. Phys. **102**, 6362 (1995).
23. N. J. Hestand and F. C. Spano, "Expanded Theory of H- and J ? Molecular Aggregates : The E ff ects of Vibronic Coupling and Intermolecular Charge Transfer," Chem. Rev. **118**, 7069–7163 (2018).
24. J. Ho and A. Partners, "Organic Lateral Heterojunction Devices for Vapor-phase Chemical Detection John C . Ho (phD thesis)," Massachusetts Institute of Technology (2009).
25. J. Quanbo, L. Julien, S. Clementine, P. Aline, L. Cecile, D. Aurelien, and B. Joel, "Metasurface for Reciprocal Spin-Orbit Coupling of Light on Waveguiding Structures Metasurface for Reciprocal Spin-Orbit Coupling of Light on Waveguiding," Phys. Rev. Appl. **10**, 1 (2018).
26. X. Yu, Y. Yuan, J. Xu, K. Yong, J. Qu, and J. Song, "Strong Coupling in Microcavity Structures : Principle , Design , and Practical Application," Opt. Devices **1800219**, 1–19 (2019).